

# Initial ground-based thermospheric wind measurements using Doppler asymmetric spatial heterodyne spectroscopy (DASH)

Christoph R. Englert,<sup>1,\*</sup> John M. Harlander,<sup>2</sup>  
John T. Emmert<sup>3</sup>, David D. Babcock<sup>4</sup>, Frederick L. Roesler<sup>5</sup>

<sup>1</sup>U.S. Naval Research Laboratory, Space Science Division, Code 7641, 4555 Overlook Avenue Southwest,  
Washington, District of Columbia 20375, USA

<sup>2</sup>Department of Physics, Astronomy and Engineering Science, St Cloud State University, 720 Fourth Avenue South,  
St Cloud, Minnesota 56301, USA

<sup>3</sup>U.S. Naval Research Laboratory, Space Science Division, Code 7643, 4555 Overlook Avenue Southwest,  
Washington, District of Columbia 20375, USA

<sup>4</sup>Artep Inc., 2922 Excelsior Springs Court, Ellicott City, Maryland 21042, USA

<sup>5</sup>Department of Physics, University of Wisconsin–Madison, 1150 University Avenue, Madison, Wisconsin 53706,  
USA

\*Christoph.Englert@nrl.navy.mil

**Abstract:** We present the first thermospheric wind measurements using a Doppler Asymmetric Spatial Heterodyne (DASH) spectrometer and the oxygen red-line nightglow emission. The ground-based observations were made from Washington, DC and include simultaneous calibration measurements to track and correct instrument drifts. Even though the measurements were made under challenging thermal and light pollution conditions, they are of good quality with photon statistics uncertainties between about three and twenty-nine meters per second, depending on the nightglow intensity. The wind data are commensurate with a representative set of Millstone Hill Fabry-Perot wind measurements selected for similar geomagnetic and solar cycle conditions.

©2010 Optical Society of America

**OCIS codes:** (010.0280) Remote sensing and sensors; (120.0280) Remote sensing and sensors;  
(280.4991) Passive remote sensing; (300.2140) Emission; (300.6190) Spectrometers;  
(300.6320) Spectroscopy, high-resolution.

---

## References and links

1. C. R. Englert, J. M. Harlander, D. D. Babcock, M. H. Stevens, and D. E. Siskind, "Doppler Asymmetric Spatial Heterodyne Spectroscopy (DASH): An innovative concept for measuring winds in planetary atmospheres," *Proc. SPIE* **6303**, 63030T (2006).
2. C. R. Englert, D. D. Babcock, and J. M. Harlander, "Doppler asymmetric spatial heterodyne spectroscopy (DASH): concept and experimental demonstration," *Appl. Opt.* **46**(29), 7297–7307 (2007).
3. J. M. Harlander, R. J. Reynolds, and F. L. Roesler, "Spatial heterodyne spectroscopy for the exploration of diffuse interstellar emission lines at far-ultraviolet wavelengths," *Astrophys. J.* **396**, 730–740 (1992).
4. G. G. Shepherd, G. Thuillier, W. A. Gault, B. H. Solheim, C. Hersom, J. M. Alunni, J.-F. Brun, S. Brune, P. Charlot, L. L. Cogger, D.-L. Desaulniers, W. F. J. Evans, R. L. Gattinger, F. Girod, D. Harvie, R. H. Hum, D. J. W. Kendall, E. J. Llewellyn, R. P. Lowe, J. Ohrt, F. Pasternak, O. Peillet, I. Powell, Y. Rochon, W. E. Ward, R. H. Wiens, and J. Wimperis, "WINDII, the wind imaging interferometer on the upper atmosphere research satellite," *J. Geophys. Res.* **98**(D6), 10725–10750 (1993).
5. C. R. Englert, M. H. Stevens, D. E. Siskind, J. M. Harlander, and F. L. Roesler, "The Spatial Heterodyne Imager for Mesospheric Radicals (SHIMMER) on STPSat-1," *J. Geophys. Res.* **115**(D20), D20306 (2010), doi:10.1029/2010JD014398.
6. J. C. Mankins, "Technology Readiness Levels: A White Paper," NASA, Office of Space Access and Technology, Advanced Concepts Office (1995) <http://www.hq.nasa.gov/office/codeq/trl/trl.pdf>.
7. J. W. Meriwether, "Studies of thermospheric dynamics with a Fabry–Perot interferometer network: A review," *J. Atmos. Sol. Terr. Phys.* **68**(13), 1576–1589 (2006).
8. J. T. Emmert, M. L. Faivre, G. Hernandez, M. J. Jarvis, J. W. Meriwether, R. J. Niciejewski, D. P. Sipler, and C. A. Tepley, "Climatologies of nighttime upper thermospheric winds measured by ground-based Fabry-Perot interferometers during geomagnetically quiet conditions: 1. Local time, latitudinal, seasonal, and solar cycle dependence," *J. Geophys. Res.* **111**(A12), A12302 (2006), doi:10.1029/2006JA011948.

Report Documentation Page			Form Approved OMB No. 0704-0188		
Public reporting burden for the collection of information is estimated to average 1 hour per response, including the time for reviewing instructions, searching existing data sources, gathering and maintaining the data needed, and completing and reviewing the collection of information. Send comments regarding this burden estimate or any other aspect of this collection of information, including suggestions for reducing this burden, to Washington Headquarters Services, Directorate for Information Operations and Reports, 1215 Jefferson Davis Highway, Suite 1204, Arlington VA 22202-4302. Respondents should be aware that notwithstanding any other provision of law, no person shall be subject to a penalty for failing to comply with a collection of information if it does not display a currently valid OMB control number.					
1. REPORT DATE <b>07 DEC 2010</b>		2. REPORT TYPE		3. DATES COVERED <b>00-00-2010 to 00-00-2010</b>	
4. TITLE AND SUBTITLE <b>Initial ground-based thermospheric wind measurements using Doppler asymmetric spatial heterodyne spectroscopy (DASH)</b>				5a. CONTRACT NUMBER	
				5b. GRANT NUMBER	
				5c. PROGRAM ELEMENT NUMBER	
6. AUTHOR(S)				5d. PROJECT NUMBER	
				5e. TASK NUMBER	
				5f. WORK UNIT NUMBER	
7. PERFORMING ORGANIZATION NAME(S) AND ADDRESS(ES) <b>Naval Research Laboratory, Space Science Division, Code 7641, 4555 Overlook Avenue SW, Washington, DC, 20375</b>				8. PERFORMING ORGANIZATION REPORT NUMBER	
9. SPONSORING/MONITORING AGENCY NAME(S) AND ADDRESS(ES)				10. SPONSOR/MONITOR'S ACRONYM(S)	
				11. SPONSOR/MONITOR'S REPORT NUMBER(S)	
12. DISTRIBUTION/AVAILABILITY STATEMENT <b>Approved for public release; distribution unlimited</b>					
13. SUPPLEMENTARY NOTES					
14. ABSTRACT <b>We present the first thermospheric wind measurements using a Doppler Asymmetric Spatial Heterodyne (DASH) spectrometer and the oxygen red-line nightglow emission. The ground-based observations were made from Washington, DC and include simultaneous calibration measurements to track and correct instrument drifts. Even though the measurements were made under challenging thermal and light pollution conditions, they are of good quality with photon statistics uncertainties between about three and twenty-nine meters per second, depending on the nightglow intensity. The wind data are commensurate with a representative set of Millstone Hill Fabry-Perot wind measurements selected for similar geomagnetic and solar cycle conditions.</b>					
15. SUBJECT TERMS					
16. SECURITY CLASSIFICATION OF:			17. LIMITATION OF ABSTRACT <b>Same as Report (SAR)</b>	18. NUMBER OF PAGES <b>15</b>	19a. NAME OF RESPONSIBLE PERSON
a. REPORT <b>unclassified</b>	b. ABSTRACT <b>unclassified</b>	c. THIS PAGE <b>unclassified</b>			

9. P. B. Hays, V. J. Abreu, M. E. Dobbs, D. A. Gell, H. J. Grassl, and W. R. Skinner, "The high-resolution Doppler imager on the upper atmosphere research satellite," *J. Geophys. Res.* **98**(D6), 10713–10723 (1993).
10. T. L. Killeen, Q. Wu, S. C. Solomon, D. A. Ortland, W. R. Skinner, R. J. Niciejewski, and D. A. Gell, "TIMED Doppler interferometer: Overview and recent results," *J. Geophys. Res.* **111**(A10), A10S01 (2006), doi:10.1029/2005JA011484.
11. J. M. Harlander, C. R. Englert, D. D. Babcock, and F. L. Roesler, "Design and laboratory tests of a Doppler Asymmetric Spatial Heterodyne (DASH) interferometer for upper atmospheric wind and temperature observations," *Opt. Express* **18**(25), 26430–26440 (2010).
12. C. R. Englert, J. M. Harlander, J. G. Cardon, and F. L. Roesler, "Correction of phase distortion in spatial heterodyne spectroscopy," *Appl. Opt.* **43**(36), 6680–6687 (2004).
13. C. R. Englert, and J. M. Harlander, "Flatfielding in spatial heterodyne spectroscopy," *Appl. Opt.* **45**(19), 4583–4590 (2006).
14. D. P. Sipler, M. A. Biondi, and M. E. Zipf, "Vertical winds in the midlatitude thermosphere from Fabry-Perot Interferometer measurements," *J. Atmos. Terr. Phys.* **57**(6), 621–629 (1995).
15. D. P. Sipler, M. E. Hagan, M. E. Zipf, and M. A. Biondi, "Combined optical and radar wind measurements in the F Region over Millstone Hill," *J. Geophys. Res.* **96**(A12), 21,255–21,262 (1991).
16. M. J. Buonsanto, J. C. Foster, and D. P. Sipler, "Observations from Millstone Hill during the geomagnetic disturbance of March and April 1990," *J. Geophys. Res.* **97**(A2), 1225–1243 (1992).
17. J. T. Emmert, B. G. Fejer, and D. P. Sipler, "Climatology and latitudinal gradients of quiet time thermospheric neutral winds over Millstone Hill from Fabry-Perot interferometer measurements," *J. Geophys. Res.* **108**(A5), 1196 (2003), doi:10.1029/2002JA009765.
18. R. E. Dickinson, E. C. Ridley, and R. G. Roble, "A three-dimensional general circulation model of the thermosphere," *J. Geophys. Res.* **86**, 1499–1512 (1981).
19. R. G. Roble, R. E. Dickinson, and E. C. Ridley, "Global circulation and temperature structure of thermosphere with high-latitude plasma convection," *J. Geophys. Res.* **87**(A3), 1599–1614 (1982).

## 1. Introduction

The Doppler Asymmetric Spatial Heterodyne (DASH) concept has recently been proposed to measure upper atmospheric winds [1,2]. The approach is identical to the concept of Spatial Heterodyne Spectroscopy (SHS) [3] except that one interferometer arm exhibits an additional optical path offset, similar to the stepped Michelson technique [4]. DASH can therefore be viewed as an optical remote sensing concept that is a hybrid of these two interferometric techniques.

Since both SHS and stepped Michelson instruments have flown successfully on Earth orbiting satellites [4,5], and DASH has been successfully demonstrated in the laboratory [2] the next logical step in the development of a possible future DASH satellite instrument was to build a brassboard DASH instrument that is capable of measuring thermospheric winds from the ground [6]. Such ground-based Doppler shift measurements, using the atomic oxygen red line emission  $\text{OI}({}^3\text{P}-{}^1\text{D})$  at  $\lambda = 630\text{nm}$ , are routinely performed at many ground stations across the globe, typically using Fabry-Perot interferometers [7,8]. A ground-based DASH instrument gives us the opportunity to demonstrate thermospheric wind measurements using an atmospheric emission feature that is suitable for space-borne measurements [4,9,10]. It also allows us to use the same instrumental setup for future, simultaneous, collocated measurements with an established ground-based Fabry-Perot or stepped Michelson instrument.

In the following sections, we describe the Redline DASH Demonstration Instrument (REDDI) and show data from the first two nights of observations taken from the Naval Research Laboratory (NRL), Washington DC (38.83°N, 77.02°W) in the summer of 2010. We discuss the analysis approach applied to the data and present the retrieved meridional and zonal wind speeds throughout the two nights. Since there are no simultaneous and collocated measurements available for this time and location, we compare these initial wind results to a set of measurements taken by a Fabry-Perot instrument at the Millstone Hill Observatory (42.62°N, 71.49°W) under approximately the same geomagnetic and solar conditions [8].

## 2. Instrument configuration

The REDDI instrument is built on a 3 ft × 4 ft aluminum optical breadboard. A photograph of the optics is shown in Fig. 1A. A schematic of the instrument is shown in Fig. 1B and details about the mnemonics used in this figure are listed in Table 1.

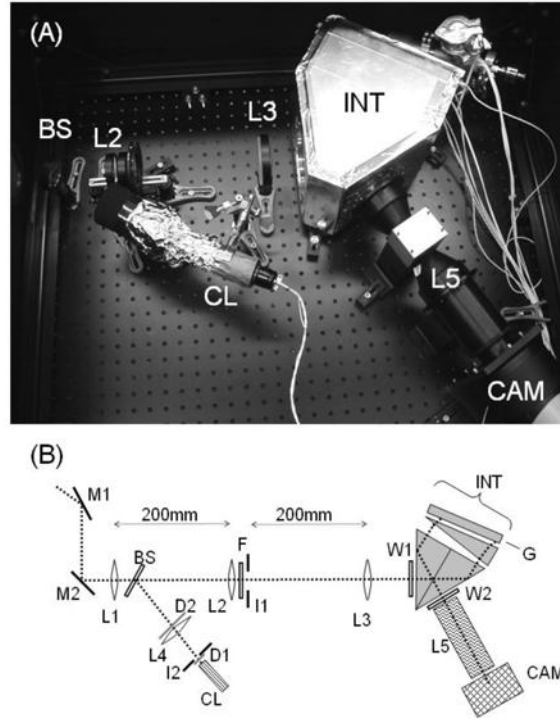


Fig. 1. (A) Picture of the main components of the REDDI instrument. (B) Schematic of the REDDI instrument. Component details are listed in Table 1.

Light enters the instrument via a pointing mirror assembly that consists of two first surface mirrors, M1 and M2. Mirror M1 is mounted on a motor driven rotation stage so that the instrument field of view can be directed to different azimuth angles at a constant elevation angle of  $35^\circ$ . The field of view on the sky is a circular cone with a half angle of about  $4.7^\circ$ . At one azimuth position, the field of view is directed to the zenith by a third, fixed mirror (not shown in Fig. 1).

The fore-optics (lenses  $L1$  to  $L3$ ) image the sky at the position of lens  $L2$  while forming an image of lens  $L1$  on the interferometer grating  $G$ . The iris  $I1$  is positioned one focal length away from lens  $L3$ , so that the diameter of the iris simultaneously controls the incident cone angle of the beam on the interferometer grating and the field of view on the sky. With this design, the sky scene is almost completely out of focus at the interferometer grating. The interference filter  $F$  is located between lens  $L2$  and iris  $I1$ . It is mounted on a rotation stage so its angle with respect to the optical axis can easily be adjusted. Since incident angles on the filter correspond to locations on the grating and the filter transmittance is a function of incident angle, we chose to align the filter perpendicular to the optical axis. This alignment minimizes the variation of the filter transmittance across the image on the grating.

A beam sampler is located between lenses  $L1$  and  $L2$  to view the neon (Ne) calibration line signal ( $\lambda_{\text{Ne}} = 630.48 \text{ nm}$ ) from a hollow cathode lamp simultaneously with the atmospheric signal. This calibration line signal is collimated and diffused before reflection on the beam sampler.

Table 1. Instrument Components		
Mnemonic	Component	Description
BS	Beam sampler	Diameter: 2 inches, 0.5° Wedge angle Fused silica, one side anti-reflection coated
CAM	CCD camera	Princeton Instruments PIXIS 2048B 2048 × 2048 pixels, 13.5μm pixel pitch Back illuminated, liquid cooled Pixel binning: 4 × 4
CL	Calibration lamp	MnNe hollow cathode lamp
D1	Diffuser	Frosted tape
D2	Holographic diffuser	Diameter: 50 mm, diffusing angle: 25°
F	Narrow band interference filter	Diameter: 2 inches Center wavelength: 630.64 nm Full width at half maximum: 1.9 nm Maximum transmittance >75% Transmittance at 630nm: 53%
G	Interferometer grating	As described by Harlander et al. [11]
I1	Iris	Mounted blade diaphragm Clear aperture ~33 mm
I2	Iris	Mounted blade diaphragm Clear Aperture ~1 mm
INT	Interferometer	DASH interferometer as described by Harlander et al. [11]
L1 & L2	Achromatic lenses	Focal length: 200 mm Diameter: 50 mm
L3	Achromatic lens	Focal length: 200 mm Diameter: 75 mm
L4	Lens	Focal length: 100 mm Diameter: 50 mm
L5	Double sided telecentric lens	Magnification: 1 × Working distance: 160mm
M1 & M2	First surface mirrors	M1 is mounted on a precision, DC motor rotation stage for azimuth pointing
W1 & W2	Interferometer enclosure windows	BK/7, antireflection coated Diameter: 100 mm

The monolithic DASH interferometer of REDDI is described in detail by Harlander et al. [11]. This particular interferometer uses a Kösters prism as a beamsplitter, rather than a cube beamsplitter which was used in previous work [2]. In this configuration the interferometer arms are parallel due to additional total internal reflections on the inside of the Kösters prism as shown in Fig. 1B. The arm with the longer path uses the thicker part of the field widening prism. In this configuration, a single field-widening prism and grating can be used to terminate both interferometer arms, which results in fewer components in the interferometer and several alignment advantages, e.g. the grating tilt and roll angles are by definition equal in both arms. In contrast to a design with two separate interferometer arms, this design couples the path difference offset between the two arms with the grating angle. However, for measuring the thermospheric red line, the optimum path difference [2] is small enough that it can be achieved with a small grating angle, which makes this particular design approach viable. We point out that for measuring other atmospheric emission lines that require a larger optical path difference (e.g. the thermospheric oxygen green line) a more conventional interferometer design that uses two separate interferometer arms is likely a better choice than a design using a Kösters prism.

The REDDI interferometer is contained in a temperature-controlled aluminum enclosure. Two strip heaters mounted on the outside of the enclosure in combination with commercially available temperature sensors and PID (proportional-integral-derivative) controllers are used to keep the aluminum walls of the container stable within  $\pm 0.1^\circ\text{C}$ . The outside of the container is lined with 12 mm thick foam board and aluminum tape for thermal insulation. The interferometer is mounted in compression at six points on the triangular faces of the

Kösters prism using lapped stainless steel interfaces, so that the interferometer is in poor thermal contact with the enclosure walls. For the measurements presented here, the interferometer enclosure is filled with one atmosphere of dry nitrogen and then sealed, so that the gas density and index of refraction are virtually independent of temperature.

The exit optic  $L5$  is a custom telecentric lens that images the fringe localization plane of the interferometer, located close to the grating, onto the detector's focal plane array. The detector (*CAM*) is a commercially available, low noise, liquid cooled CCD (charge coupled device) camera with a mechanical shutter. For the measurements presented here, the  $2048 \times 2048$  pixel array was binned  $4 \times 4$  and an image with  $512 \times 512$  elements is stored. Henceforth, these  $4 \times 4$  pixel image elements are referred to as "pixels".

### 3. Ground-based measurements

After conclusion of the initial laboratory characterization of REDDI [11], we temporarily relocated the instrument to the roof of the NRL Space Science Division building for two nights to perform ground-based thermospheric wind measurements. Due to the large amount of light pollution from the densely populated surrounding area and a scarcity of cloud-free nights during the summer months, this location is not at all optimal for this type of measurement. Furthermore, the thermal environment on the roof, where the instrument is directly exposed to the ambient atmosphere and indirect solar illumination, is far from ideal. Thus, obtaining usable wind measurements under these extremely challenging conditions represents a very powerful demonstration of the DASH technique.

The measurements were performed on the nights of May 20/21, 2010 and June 7/8, 2010. The instrument was moved to the roof in the afternoon, shielded from direct sunlight and the interferometer enclosure target temperature was set to  $30^\circ\text{C}$ . The viewing direction of the instrument was switched periodically from eastward ( $35^\circ$  elevation), to southward ( $35^\circ$  elevation), to the zenith ( $90^\circ$  elevation) with a dwell time of 310 seconds. During each of these periods a single exposure with an integration time of 300 seconds was taken. The CCD was cooled to  $-50^\circ\text{C}$ . The measurements are fully automated so that no operator intervention is needed during the night.

Figure 2 shows a measured fringe image taken in the southward direction around 21:30 EDT (eastern daylight savings time) on June 7, 2010. On the top of the image one can see the edge of the grating and a number of periodic marks that are manufactured into the grating to monitor the position of the grating image on the CCD [11]. The darker regions at the bottom corners of the image are due to non-uniform illumination of the CCD. The only correction applied to the image shown in Fig. 2 is the replacement of hot pixels and spikes with an average computed from a set of vertically neighboring pixels in the same pixel column. No darkfield, flatfield, or phase distortion correction was performed for this image [12,13].

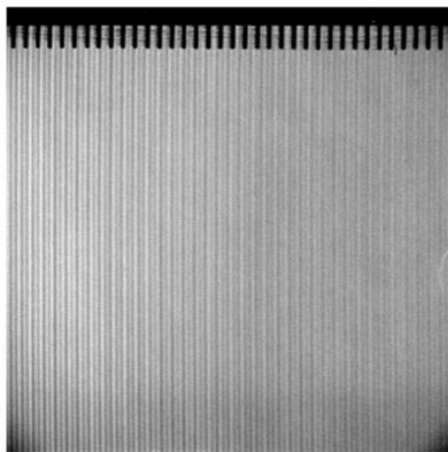


Fig. 2. Raw image, spike and hot pixel corrected, taken around 21:30 EDT of June 7, 2010 using the southward look direction ( $180^\circ$  azimuth,  $35^\circ$  elevation).

#### 4. Data analysis

After a brief, general review of the data that is recorded with a DASH type instrument, we will discuss in detail how the data from the initial REDDI thermospheric wind measurements were analyzed.

As in SHS [2,3], the detector array of a DASH spectrometer generally records an interferogram  $I(L)$  within an interval of optical path differences. An interferogram measured under ideal circumstances can be written as (Eq. (1)):

$$I(L) = \frac{1}{2} \int_0^\infty B(\sigma) \left[ 1 + \cos \{ 2\pi L (\sigma(v) - \sigma_0) \} \right] d\sigma \quad (1)$$

Where  $B(\sigma)$  is the incident spectral density and  $\sigma(v)$  is the reciprocal wavelength or wavenumber, which could be Doppler shifted with the velocity  $v$  for an atmospheric observation.  $\sigma_0$  is the Littrow wavenumber, and  $L$  is the optical path difference. Unlike a typical SHS the path difference interval ( $L_{min} < L < L_{max}$ ) sampled by a DASH spectrometer is asymmetric with respect to the zero path location ( $L = 0$ ) and may not include the zero path location. This is because the information about the Doppler shift of a broadened emission line is primarily contained within an optical path interval around an optimum, nonzero value [2]. Figure 3A illustrates this behavior using the interferogram of a single emission line. At small path differences the interferograms of a shifted and unshifted emission line are only out of phase by a very small amount so that their difference is small. At high optical path differences, where the cumulative phase difference is large, the amplitude of the interferograms is small due to the nonzero line width (self-apodization), again making the difference between the shifted and unshifted interferogram small. The path difference of optimum response depends on the line shape of the observed emission line [2]. For a single, purely temperature-broadened line, the ideal interferogram can be written as (Eq. (2)):

$$I_s(L) = C \times \left[ 1 + \cos \{ 2\pi L (\sigma(v) - \sigma_0) \} \times \exp \{ -2\pi^2 \sigma_D^2 L^2 \} \right] \quad (2)$$

Where  $C$  is a constant and  $\sigma_D$  (Eq. (3)) is the temperature-broadening parameter, which is a function of the emission line wavenumber,  $\sigma_E$ , the mass of the emitter,  $m$ , and the kinetic temperature,  $T$  ( $k$  is the Boltzmann constant):

$$\sigma_D = \sigma_E \sqrt{\frac{kT}{mc^2}} \quad (3)$$

For a purely temperature-broadened line, the path difference for which the interferogram shows the largest change for a small change in the emission line wavenumber (e.g. caused by a Doppler shift) is (Eq. (4)) [2]:

$$L_{OPT} = \frac{1}{2\pi\sigma_D} \quad (4)$$

For a thermospheric temperature of  $T = 1000$  K and the atomic oxygen red line emission at  $\sigma_E = 630.0$  nm,  $L_{opt}$  is 4.17 cm.

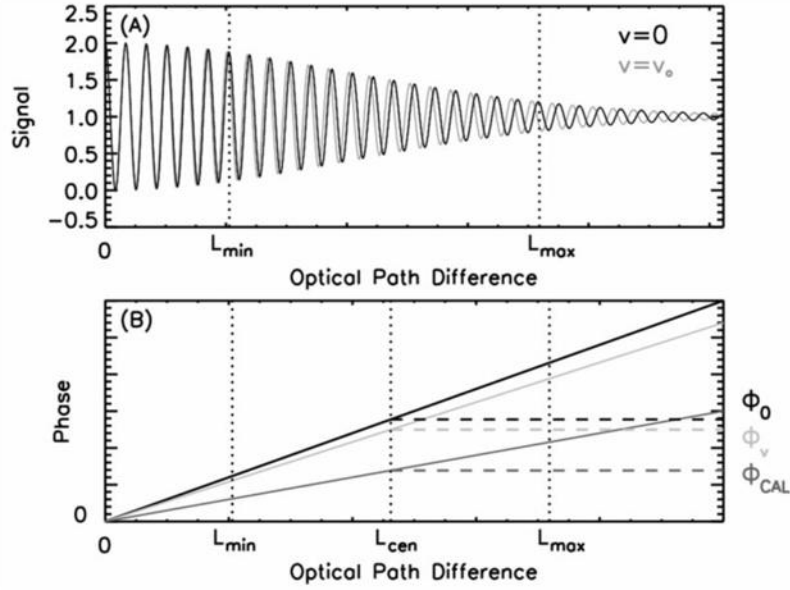


Fig. 3. (A) Ideal interferograms of a purely temperature broadened emission line with and without Doppler shift. (B) The top two solid curves are the phases corresponding to the interferograms shown in (A). The bottom curve represents the phase of a simultaneously observed calibration line (not shown in (A)). The dotted lines show an example of the path difference interval sampled by a DASH instrument and the center of the interval. The dashed lines indicate the interferogram phases at the center of the sampled path differences, with and without Doppler shift for the atmospheric emission line and for the calibration line.

The path difference interval sampled by REDDI is  $L_{min} = 1.37$  cm to  $L_{max} = 4.79$  cm. This interval is not centered on the optimum path ( $L_{opt} = 4.19$  cm for  $T = 1000$  K), since other considerations, like interferometer size, field widening, thermal stability, and the size of the path interval were also considered in the design of the interferometer [11]. Moreover, the sensitivity of the Doppler shift measurement does not change rapidly in the vicinity of the optimum path difference [2] so that the penalty for not measuring a path difference interval centered around  $L_{opt}$  is generally small. We note here that similar design trade-offs also led to departures from the optimum path differences in the design of the highly successful, stepped Michelson experiment WINDII (Wind Imaging Interferometer) which measured upper atmospheric wind profiles from low earth orbit using only either four or eight interferogram samples [4].

As shown in Eq. (2), the Doppler shift information is contained in each measured phase sample of the DASH interferogram. Using Eq. (2) and the wavenumber of a Doppler-shifted line ( $\sigma(v) = \sigma[1 + v/c]$ ), we get a simple relation between phase shift and velocity (Eq. (5)) for every optical path difference sampled by the instrument:

$$\delta\Phi(L) = 2\pi L\sigma \frac{v}{c} \quad (5)$$

Where  $c$  is the speed of light in vacuum,  $\sigma$  is the wavenumber of the non-Doppler-shifted emission line, and the non-relativistic approximation ( $v \ll c$ ) is applied. Assuming an ideal instrument, one can thus retrieve the line of sight wind speed by measuring only the phase of the target emission line. For the REDDI instrument, the phase response at the center of the sampled path differences, as illustrated in Fig. 3B ( $L_{cen} = 3.08$  cm), is about  $\delta\Phi(L_{cen}) = \Phi_0 - \Phi_v = 1$  mrad for  $\delta v = 1$  m/s.



For a real instrument designed to measure wind speeds with an accuracy of several meters per second (a wavenumber change of 1 part in  $10^8$ ) one has to account for thermal instrument drifts.

There are three main effects that must be considered for a changing instrument temperature,  $T$ . First, the change in the Littrow wavenumber ( $\sigma_0 \rightarrow \sigma_0 + \Delta\sigma_0(T)$ ) that can be caused by a thermal index change in the interferometer field widening prism or the thermal expansion of the grating [11]. Second, a thermally induced phase offset ( $\Phi(L, \sigma) \rightarrow \Phi(L, \sigma) + \Delta\Phi(T, \sigma)$ ), which is equivalent to a change in optical path in one interferometer arm but not the other, is caused for example by a temperature gradient in the instrument or by a thermoelastic distortion of the grating. Third, a thermally induced shift of the interferogram image on the CCD focal plane array can occur, which is equivalent to a slight change in the optical path difference that each pixel samples. If the optical path difference sampled by pixel  $i$  is nominally  $L_i$  then this effect causes the pixel to sample the path difference  $L_i + \Delta L(T)$ . This could be due to a thermally induced, mechanical shift of the camera. Allowing these instrument drifts, we can modify Eq. (2) to read (Eq. (6)):

$$I_s(i) = C \times \left[ 1 + \cos \{ 2\pi (L_i + \Delta L(T)) (\sigma(v) - \sigma_0 - \Delta\sigma_0(T)) + \Delta\Phi(T, \sigma) \} \times \exp \{ -2\pi^2 \sigma_D^2 (L_i + \Delta L(T))^2 \} \right] \quad (6)$$

The phase term as a function of pixel number  $i$  is therefore (Eq. (7)):

$$\Phi(i) = 2\pi (L_i + \Delta L(T)) (\sigma(v) - \sigma_0 - \Delta\sigma_0(T)) + \Delta\Phi(T, \sigma) \quad (7)$$

$\Delta L(T)$  and  $\Delta\sigma_0(T)$  are not a function of the emission line wavenumber  $\sigma$ . The additional phase term  $\Delta\Phi(T, \sigma)$  is expected to be a linear function of the observed wavenumber, so that  $\Delta\Phi_1 = \Delta\Phi(T, \sigma_1)$  and  $\Delta\Phi_2 = \Delta\Phi(T, \sigma_2)$ , where the subscripts correspond to two different wavenumbers, are related according to Eq. (8):

$$\Delta\Phi_1 = \Delta\Phi_2 \times \frac{\sigma_1}{\sigma_2} \quad (8)$$

Using the above equations, we will show below that the thermal drifts of the instrument can be tracked and corrected using the measured phase of a known emission line from a calibration source that has a wavenumber that is very close to the observed oxygen red line. The fact the lines are close in wavelength avoids any additional effects from wavenumber-dependent material properties, especially the index of refraction of the interferometer materials. According to Eqs. (7) and (8), the difference between the measured phases of the atmospheric and calibration lines can be written as (Eq. (9)):

$$\begin{aligned} \Phi_{OI}(i) - \Phi_{CAL}(i) = 2\pi (\sigma_{OI}(v) - \sigma_{CAL})(L_i + \Delta L(T)) \\ + \Delta\Phi_{CAL}(T, \sigma_{CAL}) \left( \frac{\sigma_{OI}}{\sigma_{CAL}} - 1 \right) \end{aligned} \quad (9)$$

This difference eliminates the effect of the change in the Littrow wavenumber,  $\Delta\sigma_0(T)$ , and for  $\sigma_{OI} \approx \sigma_{CAL}$  reduces the effect of the offset drift significantly.

In the following paragraphs we will examine the experimental data. We will first correct for spikes in the CCD images and perform a phase distortion correction. Subsequently, we will quantify the thermal drift terms connected to  $\Delta L(T)$  and  $\Delta\Phi(T, \sigma_{CAL})$  and make the appropriate corrections to the measured phase. Finally, we will perform a zero wind calibration using zenith measurements and derive the horizontal thermospheric wind. For clarity, some of the following figures contain data from only one of the two nights (June 7/8, 2010). Since the data look similar for both nights the same conclusions can be reached by looking at either data set.

As the first step of the data analysis, we identified hot pixels and spikes in each CCD image by comparing individual pixel values to a set of vertically neighboring pixels. Pixel

values exceeding a threshold value are replaced by an average value determined from its vertical neighbors.

Three sample interferograms recorded by REDDI during the night of June 7/8, 2010 are shown in Fig. 4. The solid black lines indicate the average of binned rows 10–450 and the green traces are data from only the center row of the binned CCD (row 256). The comparison between the single row (green) and the highly averaged data (black) shows that the fringes are straight enough and well enough aligned to the CCD columns that no major reduction in fringe contrast is observed when simply averaging the rows. We use this type of averaged data for the subsequent analyses.

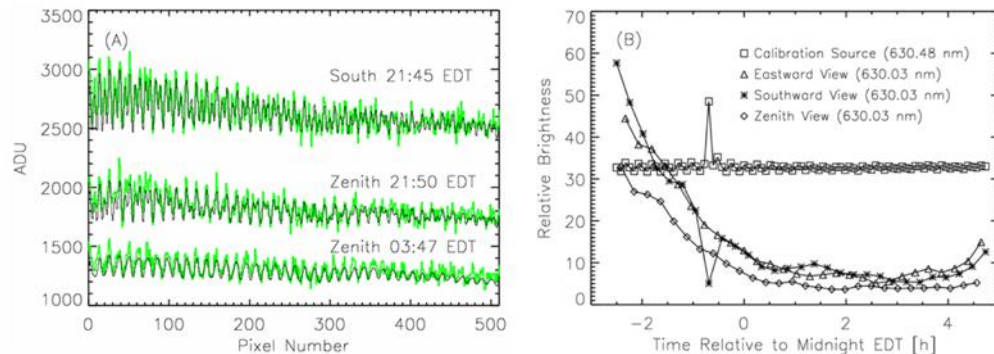


Fig. 4. (A) Sample interferograms. Green: center row of CCD (row 256). Black: average of rows 10–450. (B) Time series of brightnesses for the measurements of June 7/8, 2010 for the three viewing directions and the calibration line. A strong cloud signal is apparent around  $-0.75\text{h}$  (23:15) EDT for the southward view and the calibration signal.

All three interferograms shown in Fig. 4A clearly show a decrease in fringe contrast toward higher optical path differences (higher pixel numbers), which is due to self-apodization caused by the finite line widths and instrumental apodization [11]. The two interferograms taken at the beginning of the night clearly show a superposition of two fringe frequencies that originate from the thermospheric oxygen emission and the neon line from the calibration lamp. The oxygen line creates a fringe pattern with about 80 fringes across the focal plane, while the calibration line fringe frequency is about 42 fringes per detector width. The dimmest interferogram shown in Fig. 4A, which was taken toward the end of the night, is dominated by the Ne calibration signal due to the significant decrease in brightness of the oxygen nightglow throughout the night.

Figure 4B shows the relative brightness of the red line signal and the neon calibration line signal for the different viewing directions throughout the night. As expected, the calibration signal is largely constant, while the thermospheric signal decreases significantly throughout the night. Furthermore, the slant views (eastward and southward) show approximately equal brightness. The slant brightnesses are larger than the zenith brightnesses due to their larger slant path through the optically thin nightglow layer.

The night of June 7/8, 2010 was largely cloud free, except for around  $-0.75\text{h}$  (23:15 EDT), when the effect of a cloud is apparent in the data. The cloud causes a decrease in detected nightglow signal due to its opacity. Simultaneously, an increase in the neon signal is detected, which is likely due to light pollution scattered on the bottom side of the cloud. On a smaller scale, one can also see a periodic variation in the calibration line brightness depending on the viewing direction. We also attribute that effect to the scattered light from anthropogenic sources that are systematically different in different viewing directions. As the night progresses, the magnitude of this effect decreases, most likely because the light pollution also decreases with time. Note that the increase in the Ne signal with cloud cover and increased slant path is due to Ne *line emission* in the night sky and not continuum emission. Continuum emission is not modulated at the path differences monitored by REDDI and therefore doesn't add to the measured Ne signal, rather it only increases the noise across

the entire spectral band. The source of the additional Ne line emission is likely advertising signs in the Washington DC metro area. The data from May 20/21, 2010 do not show any obvious cloud signals like the June data; however, it cannot be ruled out that optically thin clouds were occasionally present.

Another data analysis aspect not discussed above is the effect of phase distortion. Phase distortion is generally caused by index inhomogeneity in the interferometer glasses, non-flat surfaces in the interferometer, or image distortions in the exit optics. When viewing the fringes directly as in Fig. 2, these distortions result in unequal curvature and/or spacing of the fringes. Ideally they are a spectrometer property that can be characterized and subsequently corrected if necessary [12]. To assess the phase distortion, we retrieve the phase versus pixel number for the oxygen line and the calibration line from the averaged interferograms, using the approach described by Englert et al. [2,12]. We then fit a linear function to these phase curves, using a least squares algorithm, and calculate the residuals, which represent the phase distortion of the instrument for these wavelengths [12]. The phase distortions for the neon and oxygen lines measured throughout the night of June 7/8, 2010 are shown in Fig. 5. As expected, the distortions are very similar for the two lines. We do not find any obvious change in the overall shape of the phase distortion in the data set. Note that when excluding the edges, the fringe distortion is only on the order of 200 mrad ( $\sim 3\%$  of a fringe) across the entire interferogram. To correct for the phase distortion, we average the phase distortion curves of the first 20 measurements of the night for each line (neon and oxygen) and subtract the appropriate (neon or oxygen) reference curve from all individually retrieved phase curves [12]. We use only the first 20 phase curves because the red line signal decreases significantly during the night (see Fig. 4B).

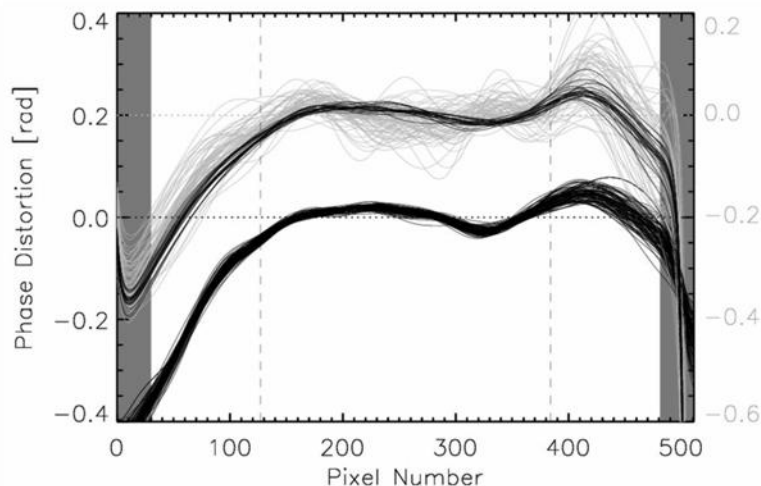


Fig. 5. Lower array of curves: Phase distortion of calibration line (Ne) interferograms (June 7/8, 2010), referenced to the left hand abscissa. Upper array of curves: Phase distortion of red line interferograms (June 7/8, 2010), referenced to the right hand abscissa. The first 20 red line measurements of the night, for which the signal is large, are highlighted in black. The vertical dashed lines indicate the horizontal limits within which a straight line was fitted to the phase data to determine the amount of distortion. These data exclude the two cloud observations shown in Fig. 4B.

We now quantify the image shift of the interferogram image on the detector, which is represented by the term  $\Delta L(T)$  in Eq. (9). The image shift is likely dominated by the thermal distortion of the breadboard itself, the exit optics and camera support structures, which are not thermally controlled and therefore are subject to the ambient temperature changes. To determine the horizontal image shift versus time, we use the periodic fiducials manufactured into the grating and shown at the top of Fig. 2. We employ a nonlinear least squares algorithm

to fit the data of a five-row average within the area of the fiducials, where one fit parameter is the horizontal shift of the fiducial pattern. The result is shown in Fig. 6B. The ambient air temperature measured near the interferometer enclosure and exit optics is shown in Fig. 6A. Figure 6B shows that this approach allows the quantification of  $\Delta L(T)$  with an uncertainty of less than about one micrometer. It also shows that the time dependence of the image shift corresponds well to the monotonic decrease in ambient temperature. This confirms that thermal distortion of the breadboard, detector, exit optics and support structures, all of which are not thermally controlled, are dominating the image shift. Due to the large volumetric heat capacity of the instrument and resulting thermal inertia, we assume that the small scale variation of the retrieved  $\Delta L(T)$  shown in Fig. 6B is predominantly due to the uncertainty of the fit result rather than a real short term image shift. For the correction of this thermal image shift, we therefore fit a low order polynomial to the data, as shown in Fig. 6B. For the oxygen line ( $\sim 80$  fringes across the CCD) a shift of  $2\text{ }\mu\text{m}$  per  $4.5^\circ\text{C}$  corresponds to a phase shift of  $32\text{ mrad}$  per  $1^\circ\text{C}$ , which corresponds to a wind speed of about  $32\text{ m/s}$  per  $1^\circ\text{C}$  for the average sampled path difference (Eq. (5)). For the difference of the oxygen and calibration line phases (Eq. (9)), the effect is about half as large, since the calibration line fringe frequency is about 42 fringes across the CCD.

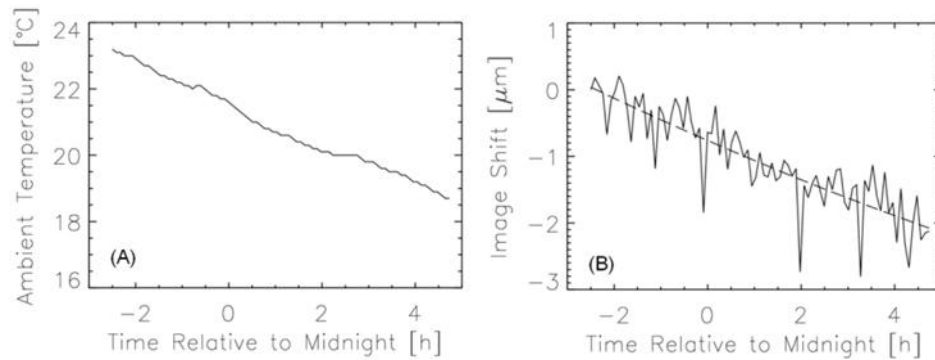


Fig. 6. (A) ambient temperature measured with sensor in air behind the interferometer enclosure. (B) image shift retrieved from grating marks (fiducials) and second order polynomial fitted to it.

The final thermal correction we examine is the phase offset, represented by  $\Delta\Phi_{\text{CAL}}$  in Eq. (9). To assess the magnitude of the offset we perform linear fits to the distortion-corrected phase curves, extrapolate the linear phase to the optical path difference of zero, and correct the result for the thermal image shift. As shown in Eq. (7), the phase offset at zero path ( $L = 0$ ) is decoupled from any change in Littrow wavenumber ( $\Delta\sigma_0(T)$ ) and from Doppler-induced wavenumber changes of the oxygen line.

The results for the oxygen and calibration lines are shown in Fig. 7 as a function of time for the June 7/8, 2010 data. We note that for the linear fit we only used phase data from the center half of the CCD (pixels 128–383), where the initial data has the lowest phase distortion and edge effects are minimized.

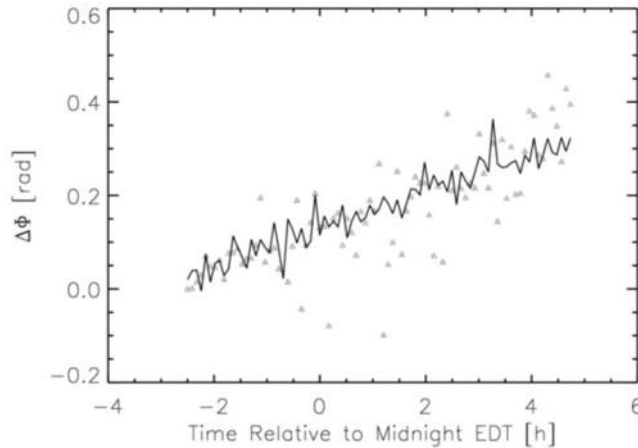


Fig. 7. Thermally induced phase offset for the calibration line (black) and the oxygen red line (gray triangles). The phase offset is extrapolated from the central half of the measured phase curves (Pixels 128–383) to avoid edge effects and residual phase distortion effects. After the initial hours of the measurement series, the phase offset extrapolation for the oxygen red line is much more uncertain than for the calibration line, due to the decreased signal level. Even though there is significant uncertainty in this extrapolated data, it supports the assumption that the phase offset for both lines is nearly identical.

Even though the phase offset data for the oxygen line has a large amount of uncertainty after the first several hours of the measurements shown in Fig. 7, the data appears to confirm that the phase offsets for the two measured lines show similar behavior, consistent with their small wavenumber difference (Eq. (8)). Moreover, the data clearly shows that the phase offset is approximately 300 mrad throughout this night, which according to Eq. (9) results in a correction that is on the order of  $300 \text{ mrad} \times (630.48 \text{ nm} / 630.0 \text{ nm} - 1) = 0.23 \text{ mrad}$  at  $L_{CEN}$ . A correction of 0.23 mrad corresponds to a line of sight wind speed of 0.23 m/s, which is negligible for these measurements. We therefore choose to not perform a phase offset correction for the data discussed here.

After addressing the thermal image shift and phase offset corrections included in Eq. (7), we can now examine the phase difference according to Eq. (9). Figure 8 shows the calibration and oxygen red line phases for the different viewing directions at  $L_{CEN}$ , which is approximately the center of the CCD. The phases at the center of the CCD (see. Figure 3A) are determined by a linear fit to the phase curves, corrected for thermal image shift. The fitted phase data excludes 30 pixels on each edge to avoid edge effects.

Figure 8 shows a significant phase drift due to a drift of the Littrow wavenumber ( $\Delta\sigma_0(T)$ ) that is apparent for both lines and all viewing geometries. We attribute this drift to the poor thermal environment on the roof, which resulted in the interferometer being slightly warmer than its thermally stabilized enclosure at the beginning of the night. According to the laboratory characterization of the interferometer, a calibration line phase drift of 100 mrad at  $L_{CEN}$  due to a Littrow wavenumber drift corresponds to an interferometer temperature change of about 0.08°C. Note that this thermal effect is fundamentally different from the image shift discussed earlier. The image shift is dominated by the thermal distortion of REDDI components that are not thermally controlled and thus are subject to a temperature change of several Kelvin throughout the night (see Fig. 6A). The thermal drift of the Littrow wavenumber is caused by the thermal drift of the interferometer, which is on the order of one tenth of a Kelvin.

In order to determine the phase that corresponds to a line of sight wind speed of zero, we use zenith measurements under the assumption that the vertical wind in the red line night glow layer is negligible [14]. As shown in Fig. 8, we shifted the calibration line phases to match the zenith observation in order to obtain a high signal-to-noise zero-wind calibration.

One could also use the zenith measurements themselves, but due to the much smaller signal their uncertainty is much higher than that of the calibration line, as shown in Fig. 8.

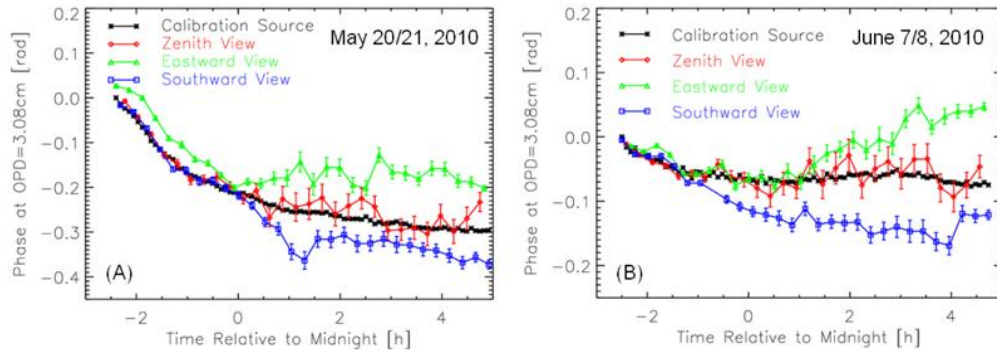


Fig. 8. (A) and (B): Retrieved phases, corrected for phase distortion and image shift on the CCD. Each phase value is the value of a linear fit to the data at the center of the path difference interval. The absolute phase of the calibration source phase is shifted so that the first phase point is zero. The sky measurements are shifted so that the first 10 zenith phases overlap with the calibration source phases. This way, the calibration phases, rather than the zenith phases, which have significantly larger uncertainties can be used for the zero wind calibration. Note that the error bars shown here are simulated, one sigma shot noise contributions. The uncertainties due to shot noise generally increase with time, due to the decreasing airglow brightness, as shown in Fig. 5. The one observation contaminated by the cloud on July 7, 2010 is not included in this data.

The differences between the phases of the sky measurements and the shifted calibration line phases shown in Fig. 8 are proportional to the line of sight wind speeds, following Eqs. (9) and (5). To convert the phase differences to line of sight wind speeds we use  $\delta\Phi/\delta v = 1.02 \text{ mrad (m/s)}^{-1}$ . To convert the line of sight winds to horizontal winds we multiply the line of sight winds with the secant of the field of view elevation  $\sec(35^\circ) = 1.22$ , which assumes no vertical wind component. The resulting horizontal wind speeds are shown and discussed in the following section.

## 5. Discussion of wind results

Figure 9 shows the initial REDDI horizontal wind measurements from May 20/21, 2010 and June 7/8, 2010 including the propagated shot noise error, which is the dominant statistical uncertainty throughout most of the night. The accuracy of the zero wind calibration is estimated to be on the order of 10 m/s. The one observation that was contaminated by a cloud on June 7, 2010 around 22h local solar time (see Fig. 4), was removed from the data shown in Fig. 9. Overplotted in Fig. 9 are measurements from the nearby Millstone Hill Fabry-Perot Interferometer [15–17]. The data were selected to approximate the geophysical conditions of the REDDI measurements: Day of year 110–160,  $K_p \leq 3.3$ ,  $F10.7 \leq 90$ .

The data from Millstone Hill shown in Fig. 9 were taken between 1994 and 1997 and were measured with a scanning Fabry Perot, resulting in uncertainties between 13–200 m/s, with an average of 57 m/s. The black circles show averages of the Millstone Hill Fabry Perot data in 2-hour local time bins. The black vertical bars denote the standard deviations of the Millstone Hill data, which are dominated by geophysical variability and therefore represent the range of wind speeds expected for these geophysical conditions.

Current Fabry-Perot technology can achieve significantly lower uncertainties; however, we chose to show this data in comparison because it is the best available match to the geophysical conditions of the REDDI data and because most of the variability in the Fabry-Perot data is geophysical rather than instrumental.

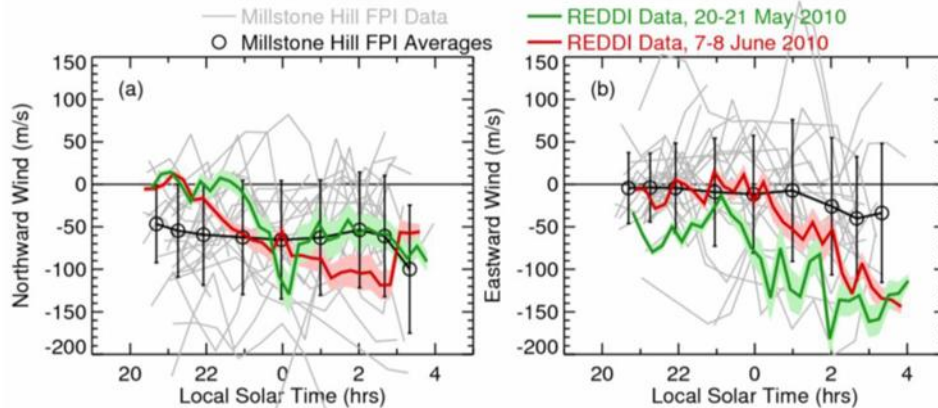


Fig. 9. The green lines show REDDI wind measurements taken on the night of 20/21 May, 2010. The red lines show REDDI wind measurements taken on the night of 7/8 June, 2010. The lighter shading depicts an estimate of the  $1\sigma$  photon shot noise uncertainty of the measurement, which dominates the error in the wind measurements throughout most of the night. Both dates were geomagnetically quiet ( $K_p = 2$ ) and near solar minimum ( $F_{10.7} \approx 70$ ). Panel (A) shows the meridional component (positive northward) of the horizontal wind, and panel (B) shows the zonal component (positive eastward). The location of the meridional wind measurement is about ( $35.5^\circ\text{N}$ ,  $77^\circ\text{W}$ ), and that of the zonal wind measurement is about ( $39^\circ\text{N}$ ,  $73^\circ\text{W}$ ). The gray lines show 30 nights, between 1994 and 1997, of measurements by the Millstone Hill Fabry-Perot Interferometer [15–17]. The data were selected to approximate the geophysical conditions of the REDDI measurements: Day of year 110–160,  $K_p \leq 3.3$ ,  $F_{10.7} \leq 90$ . The location of the Millstone Hill observatory is about ( $43^\circ\text{N}$ ,  $71^\circ\text{W}$ ). The black circles show averages of the Millstone Hill data in 2-hour local time bins; error bars denote the standard deviation.

As a result of pressure gradients induced by solar heating [18], mid-latitude thermospheric winds are generally poleward/westward during the day and equatorward/eastward at night. Polar circulation patterns created by momentum transfer from ions to neutrals can also influence mid-latitude winds [19]. During summer months, zonal winds at upper mid-latitudes are typically westward at all local times, with a minimum magnitude near dusk. The REDDI winds appear to be commensurate with the nearby Millstone Hill measurements under similar conditions, generally being within one standard deviation of the average Millstone Hill winds. The REDDI zonal winds show the same general pattern of increasingly westward values as the night progresses. The REDDI meridional winds agree well overall with the Millstone Hill averages; the southward feature in the May 20/21, 2010 data near midnight could be a signature of a passing atmospheric gravity wave.

## 6. Conclusion

We presented the first thermospheric red-line wind measurements using a Doppler Asymmetric Spatial Heterodyne spectrometer. The measurements were conducted during two nights in the summer of 2010 from Washington, DC using a breadboard instrument. The instrument included a monolithic DASH interferometer based on a Kösters prism and except for the interferometer itself, the experiment was not thermally controlled. The observations were made with the instrument exposed to the outside environment. Moreover, due to the vicinity of a major metropolitan area, the measurements were subject to a significant amount of light pollution. Despite these challenging conditions, the results are of good quality and present a powerful demonstration of the DASH technique. One major contribution to the quality of the results are the simultaneous calibration line measurements that were used to quantify and correct the thermal drift of the instrument.

The wind data were compared to and found to be commensurate with a representative set of Millstone Hill Fabry-Perot wind measurements selected for similar geomagnetic and solar cycle conditions.

## 7. Outlook

The DASH technique is an innovative approach for remote sensing of atmospheric winds. Future applications of DASH instruments may include instruments on ground-based, airborne, balloon-borne, and space-borne platforms. Each application will have its own set of requirements that should be considered in the individual instrument design and operation. For example, a space-based instrument in low earth orbit will have an integration time limitation that is driven by the horizontal resolution requirement, it will be able to take advantage of the limb path enhancement of the airglow and, with adequate baffling, the background contribution to the measured signal will be significantly reduced compared to the measurements discussed here. Fundamentally, the performance of a DASH device is expected to be similar to that of a stepped Michelson device [4], but DASH has no moving parts, allows the simultaneous observation of one or more calibration lines, has relaxed fabrication tolerances [11], provides additional immunity to ghosts and background features [2], and enables the simultaneous observation of more than one atmospheric emission line which can be particularly useful when observing lines that are closely spaced, such as molecular emission lines.

## Acknowledgements

This work was supported by the Office of Naval Research. The authors would like to thank Ronen Feldman, Andrew N. Straatveit, John F. Moser, W. Layne Marlin, Patrick B. Bell, David E. Siskind, Thomas J. Immel, Stephen B. Mende, and Todd R. Pedersen for their assistance and/or valuable discussions. The Millstone Hill FPI wind data were obtained from the NSF-supported CEDAR database at the National Center for Atmospheric Research.